Science of the Total Environment 891 (2023) 164659

Contents lists available at ScienceDirect

Science of the Total Environment

journal homepage: www.elsevier.com/locate/scitotenv

A strong short-duration convection near Poyang Lake in daytime of warm season

Haibo Zou [a,b,c,*], Miaoxia Tian [a], Anning Huang [d], Landi Zhong [e], Shanshan Wu [f]

[a] Key Laboratory of Poyang Lake Wetland and Watershed Research of Ministry of Education & School of Geography and Environmental Science, Jiangxi Normal University, Nanchang 330022, China
[b] Meteorological Sciences Institute of Jiangxi Province, Nanchang 330046, China
[c] Key Laboratory of Natural Disaster Monitoring, Early Warning and Assessment of Jiangxi Province, Nanchang 330022, China
[d] School of Atmospheric Sciences, Nanjing University, Nanjing 210000, China
[e] Nanchang Meteorological Bureau, Nanchang 330046, China
[f] Jiangxi Climate Center, Nanchang 330046, China

HIGHLIGHTS

- PL plays an important role in the development of the convection near the west shore of Poyang Lake (PL) on 4 May 2020.
- When the convection approaches the west shore of PL, its rapid enhancement is mainly associated with lake-land breeze.
- When the convection enters the main body of PL, its rapid weakening is mainly induced by PL's cooling and lake-land breeze.
- The local topography (Meiling) to the southwest of PL plays an important role in the initiation of the convection.

GRAPHICAL ABSTRACT

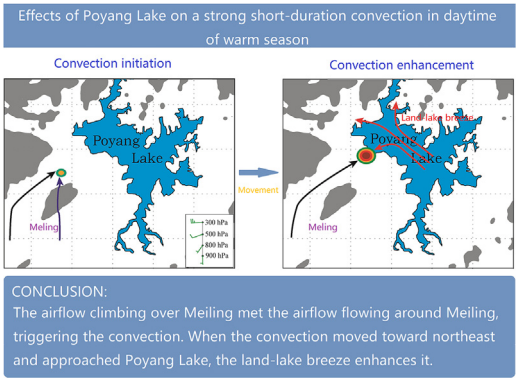

ARTICLE INFO

Editor: Fernando A.L. Pacheco

Keywords:
Poyang Lake
Convection
Lake-land breeze
Atmospheric stability

ABSTRACT

Poyang Lake (PL), the biggest freshwater lake in China, is situated in the East Asian Monsoon region, and has an important impact on local convection. In general, PL can result in convection in local region when it is a heat source in nighttime of warm season. However, at around noon on 4 May 2020 (PL is a cold source), a convection was triggered about 20 km west of PL, and rapidly enhanced and resulted in lightning when approaching PL, and then quickly weakened and disappeared after entering the main body of PL. In order to explore the convection formation, several observational data and the Weather Research and Forecasting model were applied in this study. Results show that when the convection approaches PL, its rapid enhancement is induced by PL, and after entering the main body of PL, its quick weakening is also resulted from PL. However, the initiation of the convection is mainly induced by the local topography west of PL under a favorable large-scale background. Mechanism analysis indicates that the strong low-level convergence near the west shore of PL associated with lake-land breeze is responsible for the rapid enhancement of the convection, and the low-level divergence over the main body of PL associated with the lake-land breeze and the increase of the low-level stability induced by cooling of PL jointly result in the quick weakening of the convection. The prevailing southerly wind in low level passes through the local topography (Meiling Mountain) west of PL, and

* Corresponding author at: Key laboratory of Poyang Lake wetland and watershed research ministry of education & School of Geography and Environmental Science, Jiangxi Normal University, Nanchang 330022, China.
E-mail address: zouhaibobo@sohu.com (H. Zou).

http://dx.doi.org/10.1016/j.scitotenv.2023.164659
Received 18 March 2023; Received in revised form 22 May 2023; Accepted 2 June 2023
Available online 4 June 2023

is divided into southwesterly wind (flow around Meiling) and southerly wind (flow over Meiling), and they converge in the north of Meiling, triggering the convection. This study is not only important to deepen the understanding of PL affecting regional weather, but also helpful for improving the refined forecasting of convection near PL.

1. Introduction

Lake is an important moisture source of low-level atmosphere, and featured by unique physical properties, e.g., small surface roughness, high thermal inertia and low albedo (Wu et al., 2019, 2020). Such unique physical properties can change the surface thermal conditions, the water and energy balances near a lake (Nordbo et al., 2011; Ma et al., 2014; Stepanenko et al., 2014), modifying the weather and climate in the region near the lake. In winter, some lakes in North America (such as the Great Lakes, the Great Salt Lake, Figer Lakes) can induce strong convections, resulting in short-term heavy rainfall, blizzard and thunder and lightning (Carpenter, 1993; Nicosia and Ostuno, 1999; Steiger et al., 2009), threatening the life and property safety of residents near the lakes. Such convection (induced by lake) is known as the lake-effect convection, and frequently occurs over lakes and their nearby areas in North America in winter time (Dockus, 1985; Kristovich and Spinar, 2005; Alcott et al., 2012; Laird et al., 2016). Correspondingly, its forecasting skill, climatical characteristics, physical mechanism and simulation have also been investigated in depth (Hjelmfelt, 1990; Miner and Fritsch, 1997; Kristovich and Spinar, 2005; Wright et al., 2013; Xiao et al., 2018; Huziy et al., 2021).

In fact, the Great Lakes (>10,000 km^2) in North America cannot only produce the convection (i.e., lake-effect convection), but also enhance the existing convection passing through it. For example, a lake in the Great Lakes region can enhance the convection originating from an upstream lake (Rose, 2001; Rodriguez et al., 2007; Kristovich et al., 2018; Lang et al., 2018), and increase the precipitation and change the moving speed of storms crossing it in wintertime (Angel and Isard, 1998; Schroeder et al., 2006; Owens et al., 2017). In addition to producing and enhancing convection, a lake in North America can also weaken the storms crossing it (Metz, 2011; Workoff et al., 2012). The impact of the lakes in North America on storms largely depends on the lake temperature (Ruhf and Cutrim, 2003; Kristovich and Spinar, 2005; Workoff et al., 2012). When a lake is obviously warmer than the nearby land (e.g., wintertime), the air can absorb heat and water vapor from the lake, destabilizing the stable stratification of the low-level atmosphere, promoting the formation and enhancement of convection over the lake and its nearby area (Kristovich and Spinar, 2005). In contrast, when a lake is obviously cooler than the surrounding land (e.g., summertime), the lake can absorb heat from the overlying air, strengthening the stable stratification of the low-level atmosphere, preventing the convection formation and weakening the crossing convection (Workoff et al., 2012).

Recently, with the improvement of weather monitoring (particularly, the operational application of new generation Doppler weather radar) and simulation capabilities, some lakes in China have also been reported to affect regional convection or precipitation. For example, the Qinghai Lake (approximately 4500 km^2), which is the largest lake in China, can obviously enhance the regional precipitation at nighttime from July to December (Su et al., 2019). The Poyang Lake (PL, approximately 3800 km^2), which is the biggest freshwater lake and the second largest lake in China, can produce lake-effect convection and enhance crossing convection at nighttime (Zou et al., 2020, 2022), and also weaken the crossing convection at daytime in warm season (Fu et al., 2013). Similarly, the overall effect of Taihu Lake (the third largest freshwater lake in China with an area of about 2400 km^2) on local summer convective precipitation is negative during daytime and positive during nighttime (Gu et al., 2016). The Nam Co Lake, which is located in Tibetan Plateau and is the second largest salt water lake in China, can enhance obviously the accumulated precipitation and snow in the downwind area from November to December (Xu et al., 2018; Dai et al., 2020). Moreover, the lake clusters over Tibetan Plateau can suppress the short-duration rainfall during daytime, and strengthen the convective rainfall during nighttime in summer (Wu et al., 2019; Zhao et al., 2022).

The above researches indicate that lakes in China (e.g., PL, Taihu Lake, lakes cluster over Tibetan Plateau) can usually suppress convection during the daytime, and strengthen/induce convection during nighttime in the warm season (May–September). However, lakes in North America are rarely reported to strengthen/include convection in warm season (especially for summer). The major reason may be that lakes in North America are more norther, larger and deeper than lakes in China, resulting in low lake surface temperatures in summer. For instance, PL is near 29.1°N (which is >1000 km south of the Great Lakes in North America) and is situated in the East Asian Monsoon region. Affected by the East Asian summer monsoon, the air over PL and its surrounding areas have more water vapor and stronger unstable energy compared to that over the area with high latitude (e.g., lakes in North America) or high altitude (e.g., lakes in Tibetan Plateau), which may induce the effect of PL on local weather more sensitive and complex (Zou et al., 2020, 2022).

However, in practice, a convection was triggered about 20 km west of PL at around noon on 4 May 2020, and rapidly enhanced and resulted in lightning when approaching PL, and then quickly weakened and disappeared after entering the main body of PL. The strong short-duration convection occurred near the shore of lake during daytime of warm season, and was obviously different from the previous studies (Workoff et al., 2012; Fu et al., 2013; Wu et al., 2019; Su et al., 2019; Zou et al., 2020). How does this convection form? Is the strong short-duration convection related to the PL? At present, these problems are not yet clear, and revealing these problems can deepen the understanding of PL affecting regional weather and is helpful for improving the forecasting of convection near PL. Therefore, in this study, we will examine the convection, and explore the effects of PL. The remainder of this paper is organized as follows. Section 2 describes PL and data used in this study, while Section 3 overviews the strong short-duration convection. The observational analysis is presented in Section 4, while the simulation analysis is depicted in Section 5. Possible mechanisms are analyzed in Section 6, and conclusions are given in Section 7.

2. PL and data

2.1. PL and its surrounding topography

PL, which is the biggest freshwater lake and the second largest lake in China, is located in the north of Jiangxi Province and next to the south bank of the Yangtze River (Fig. 1a). The latitude of its main body is near 29.1°N, and the location is >1000 km south than the Great Salt Lake and Great Lakes in North America. PL occupies an area of approximately 3800 km^2 (which is slightly less than that of Great Salt Lake), with the main body orienting from northwest to southeast, an average width of about 30 km (the maximum width is approximately 75 km), and the length of about 130 km (Fig. 1b). It is a relative shallow lake with the mean depth of about 6 m in the warm season (Shankman et al., 2012; Li et al., 2017), but it is deeper than Taihu Lake (about 1.9 m) in China (Wang et al., 2014). Moreover, several steeply sloped mountains (Lushan, Mufu Mountain and Meiling) with an altitude of above 500 m are located to the west and northwest of PL (Fig. 1b).

2.2. Data and processing

In this study, the radar data observed by the China New Generation of Doppler Weather Radar (CINRAD) with the S band of type A (named CINRAD-SA) in Nanchang City (NANC, which is the capital of Jiangxi Province) is used to describe the evolution of convection near PL, and the radar

station is about 30 (100) km from the southwest (northeast) shore of PL (Fig. 1b), favorable for detecting the convection over PL and its shores clearly (Zou et al., 2022). The hourly conventional meteorological observation data (including the temperature, dew-point temperature, wind direction and speed) at 15 automatic weather stations around PL (Fig. 1b) are applied to analyze the near-surface ambient condition. The lighting data collected by Lightning location system of Active Directory Topology Diagrammer in Jiangxi, China, which is comprised of 11 lightning detection stations (Duan et al., 2020), are also used to depict the convection development over PL and its nearby areas. All the radar data, conventional meteorological observation data and lighting data on 4 May 2020 are provided by the Nanchang Meteorological Bureau in China.

The 1 km resolution land surface temperature data product MYD11A1 at 13:00 local solar time (LST) on 3 and 4 May 2020, which is produced by the Aqua satellite platform with the Moderate Resolution Imaging Spectroscopy (MODIS) instrument, is employed to exhibit the lake surface temperature of PL. The detailed introduction (including download) of MODIS MYD11A1 can be found at https://modis.gsfc.nasa.gov/data/dataprod/mod11.php. The fifth-generation European Centre for Medium-Range Weather Forecasts (ECMWF) atmospheric reanalysis (ERA5), including 37-level air pressure, temperature, humidity, and winds with a horizontal resolution of 0.25° × 0.25° at the temporal resolution of 1 h on 4 May 2020, are utilized to examine the upper air ambient condition, and it is available at the website https://climate.copernicus.eu/climate-reanalysis. The National Centers for Environmental Prediction (NCEP) Final (FNL) data on 3 and 4 May 2020, with a horizontal resolution of 1° × 1° and the temporal resolution of 6 h, are used as the boundary and initialization conditions of the Weather Research and Forecasting (WRF) model, and obtained from https://rda.ucar.edu/datasets/ds083.2/index.html.

This radar data of NANC is volume scan data in polar coordinates, with about 1 km range resolution, about 1°azimuth resolution and nine elevation angles (0.5°, 1.5°, 2.4°, 3.4°, 4.3°, 6.0°, 9.9°, 14.6° and 19.5°). Meanwhile, the radar data are often contaminated by non-meteorological echoes such as ground clutters and biological echoes. Therefore, an improved quality control method of radar reflectivity (Zou et al., 2018) is used to remove the non-meteorological echoes, and then the nearest-neighboring interpolation method in the range-azimuth plane and linear interpolation method in the vertical direction are employed to convert the radar data from polar coordinates to 3D Cartesian coordinates with a horizontal resolution of 0.01° × 0.01° and a vertical resolution of 0.5 km.

3. Overview of the short-duration strong convection

During 13:30–15:30 LST on 4 May 2020, a strong isolated convection occurred over the west shore of PL and the adjacent areas. Specifically, at 13:51 LST, a small convection cell with the maximal reflectivity of about 40 dBZ was presented near Yongxiu (YX) which was about 30 km away from the west shore of PL (Fig. 1b and Fig. 2a). Subsequently, the convection cell strengthened slowly and moved toward the northeast direction gradually. By 14:09 LST, the intensity of the convection increased by about 5 dBZ with a maximal reflectivity of about 45 dBZ and its location was about 10 km from the west shore of PL (Fig. 2b). After that, the convection continued to move toward the northeast and enhanced rapidly.

By 14:27 LST, the convection arrived at the west shore of PL, and its maximal reflectivity was >55 dBZ, developing into a quite strong convection (Fig. 2c). Meanwhile, the coverage of reflectivity exceeding 45 dBZ has increased by about 10 times compared with that at 14:09 LST (Fig. 2b-2c). At this moment, the cross section of reflectivity along 29.1°N (i.e., the black solid line in Fig. 2c) showed that the echoes with reflectivity of about 20 dBZ have stretched up to the height of about 12 km (Fig. 2f). Correspondingly, lightning with a current of about −14 kA occurred near the vicinity of the west shore of PL (i.e., the white cross symbol in Fig. 2c). Subsequently, the convection continued to move toward northeast, and after the main body of the convection entered into PL, its intensity began to weaken quickly (Fig. 2d). By 15:21 LST, the convection has moved into the northwest part of PL with the maximal reflectivity decreasing to below 40 dBZ (Fig. 2e). About 10 min later, the convection disappeared over PL. The evolution of radar reflectivity indicates that the convection is remarkably strengthened when it is close to the west shore of PL, and rapidly decreased and disappeared when it enters into PL completely. Fig. 3a shows the averaged radar reflectivity from 13:30 LST to 15:30 LST on 4 May 2020. The mean reflectivity of >5 dBZ is banded with the northeast-southwest orientation, extending from about 20 km southwest to about 20 km northeast of the west shore of PL (Fig. 3a). This further suggests that the convection is developed rapidly when it is close to PL and weakened or disappeared quickly when it enters the main body of PL, and it is a short-duration and strong convection.

4. Observational analysis

4.1. The large-scale background

At 13:00 LST on 04 May 2020 (i.e., approaching the onset of the strong short-duration event), a 500-hPa trough was located over Southwest China, with the trough axis (dashed line) extending from northwestern Indochina Peninsula to the southeastern Tibetan Plateau (Fig. 4a). The West Pacific subtropical high (WPSH) controlled the South China Sea, with the west-ridge point of the geopotential height contour of 5910 gmp situating near (15°N, 95°E). PL (red rectangle) was situated to the north of WPSH, and near the ridge in front of the 500-hPa trough axis (Fig. 4a). At 925 hPa,

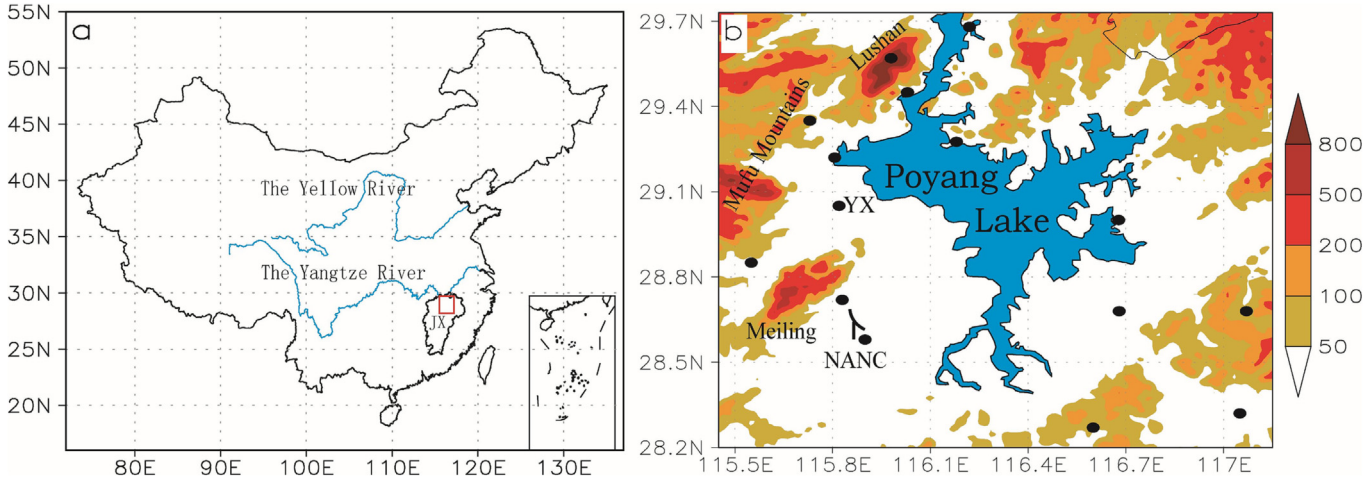

Fig. 1. (a) The location of PL in China. (b) The area of PL (blue shaded), and the surrounding topography (gray shaded; m; see color bar on the right), the temperature and rainfall observation stations (filled circles), and the radar stations in Nanchang (NANC) City. The blue lines in (a) denote rivers.

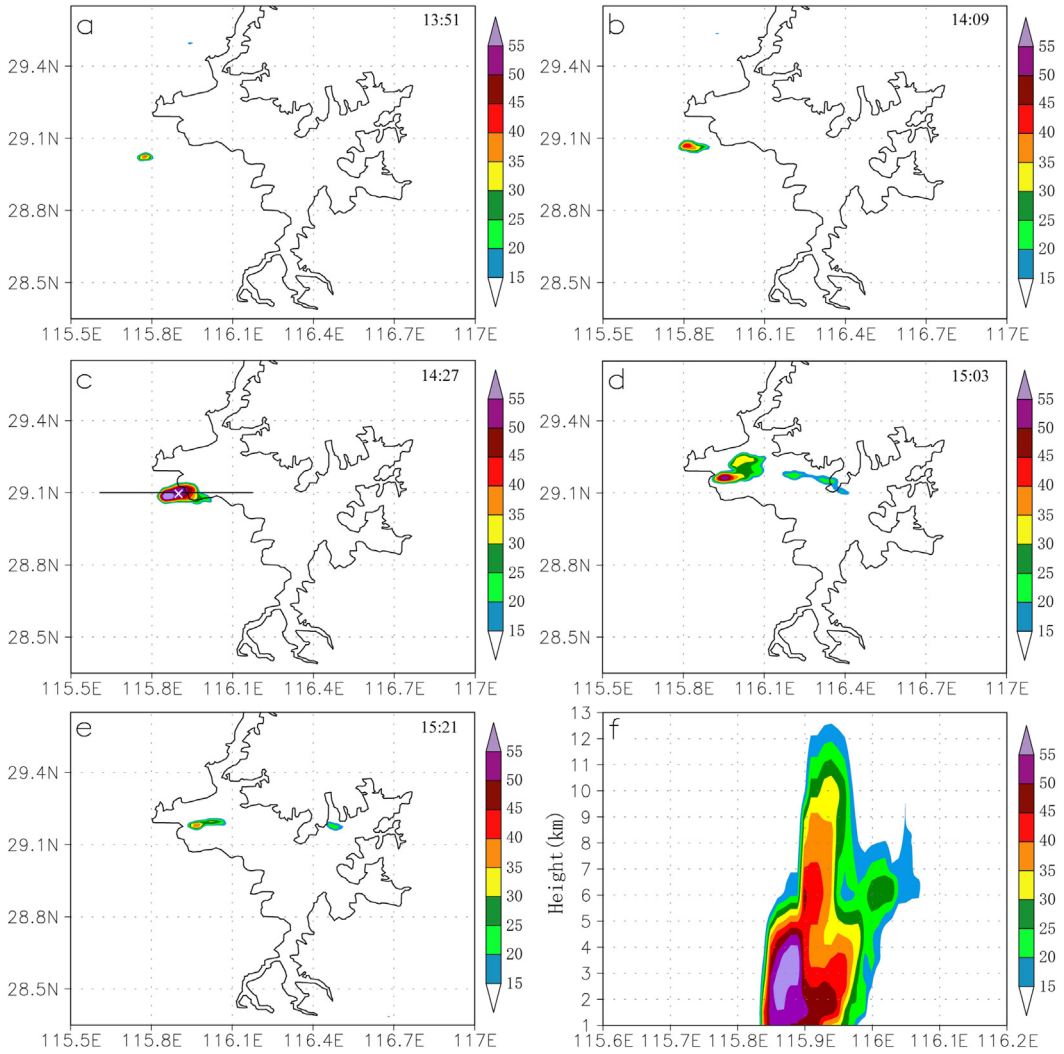

Fig. 2. Composite radar reflectivity (shading: dBZ) detected by NANC radar at (a) 13:51 LST, (b) 14:09 LST, (c) 14:27 LST, (d) 15:03 and (e) 15:21 LST on 4 May 2020. (f) The cross section of reflectivity along the black solid line in (c). The black curve denotes the boundary of PL, and the white symbol of "×" in (c) indicates the location of lightning.

the southwesterly wind jet prevailed over South China, and PL was located at the northeast edge of the jet and controlled by southerly wind and wet advection (Fig. 4b). Noted that the low-level jet may play a favorable condition for the development of the strong short-duration convection through large-scale moisture transport (Du and Chen, 2019).

Fig. 4c shows the vertical profiles of air temperature and dewpoint over YX (29°N, 115.75°E; i.e., the location of convection initiation) at 13:00 LST on 04 May 2020. The air temperature profile below 900 hPa was parallel to the dry-adiabatic line, while that above 900 hPa was situated between the moist-adiabatic line and the dry-adiabatic line. Unlike the air temperature, the dewpoint hardly changed with height below 900 hPa, and rapidly decreased above 900 hPa, but increased above 500 hPa (Fig. 3c). This implies that relatively moist ambient appears near 900 hPa (small temperature-dewpoint difference), and relatively dry ambient occurs near 500 hPa (large temperature-dewpoint difference). Such ambient produces a significant convectively unstable layer (θ_{se} increasing with height) between 900 and 600 hPa, with a large convective available potential energy (CAPE) of 1719 J (Fig. 3d), favoring the development of convection. It can also be seen from Fig. 4c that the temperature-dewpoint difference at near surface is >10 °C, implying a relatively dry ambient, which is responsible for the relatively high lifting condensation level (LCL) and level of free convection (LFC). The high LCL and LFC produce a convective inhibition (CIN) of 5 J (Fig. 3d), which implies that the near-surface air requires a certain intensity of upward motion to overcome CIN to trigger convection. Moreover, the vertical evolution of wind over YX shows that there are weak (<2 m s^{-1}) southerly winds below 900 hPa and weak southwesterly winds between 900 and 400 hPa (Fig. 4d). The movement of the convection toward northeast is mainly induced by the steering of the southwesterly winds between 900 and 400 hPa.

4.2. Near-surface temperature, humidity and wind

Affected by the underlying surface in a lake region, the near-surface temperature, humidity and wind may be obviously different from the ambient temperature, humidity and wind, and lake surface temperature is a key factor of lake affecting them (Carpenter, 1993; Steenburgh et al., 2000; Zou et al., 2022). There were no measurements of lake surface temperature in PL during this event. Recently, satellite remote sensing technologies have been developed rapidly (Li et al., 2021; Zhang et al., 2022; Dibs et al., 2023), and widely used to monitor the land surface temperature (Javadinejad et al., 2020; Li et al., 2021; Dibs et al., 2023). Fig. 5a shows the MYD11A1 land surface temperature at 13:30 LST on 3 May 2020. It was noted that there were no valid data over PL in MYD11A1 on 4 May 2020 due to convection. However, PL was always in front of the 500-hPa ridge from 08:00 LST on 3 to 13:00 LST on 4 May 2020 with sunny weather, and there was also no obviously low-level temperature advection and precipitation affecting PL region from 1 May to 3 May 2020. Therefore, the land surface temperature over PL region at 13:00 LST on 4 May 2020

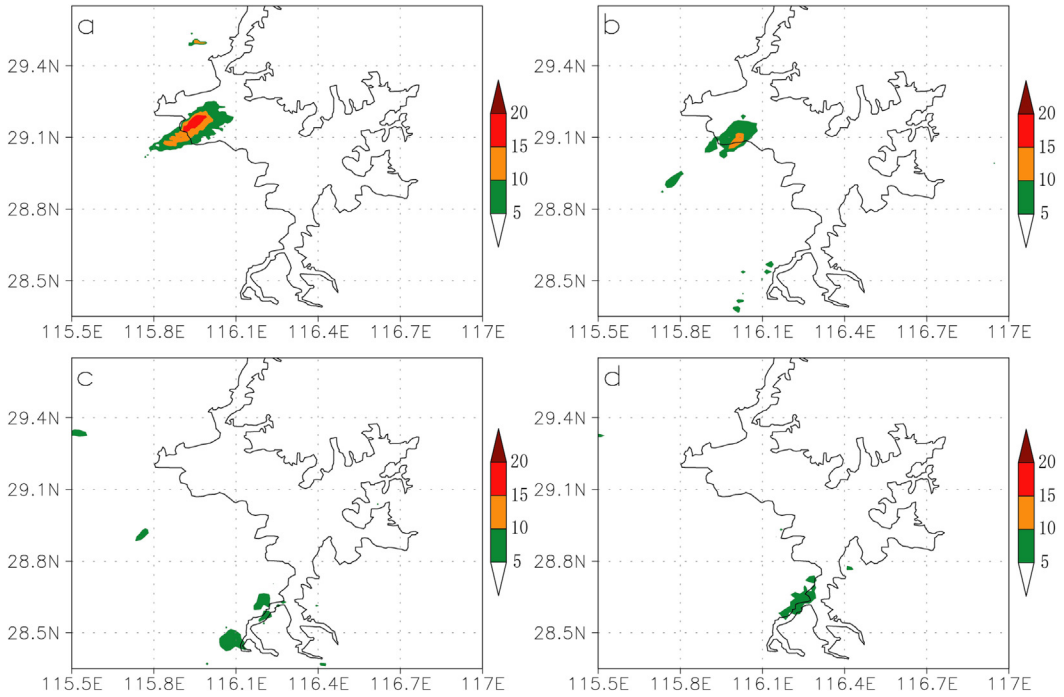

Fig. 3. The mean reflectivity (shading: dBZ) during 13:00–15:30 LST on 4 May 2020 obtained from (a) observation of NANC radar, (b) numerical experiment with PL and Meiling Mountain, (c) numerical experiment without PL (PL is replaced by arable land) and (d) numerical experiment without PL and Meiling Mountain (the altitude is decreased to below 30 m).

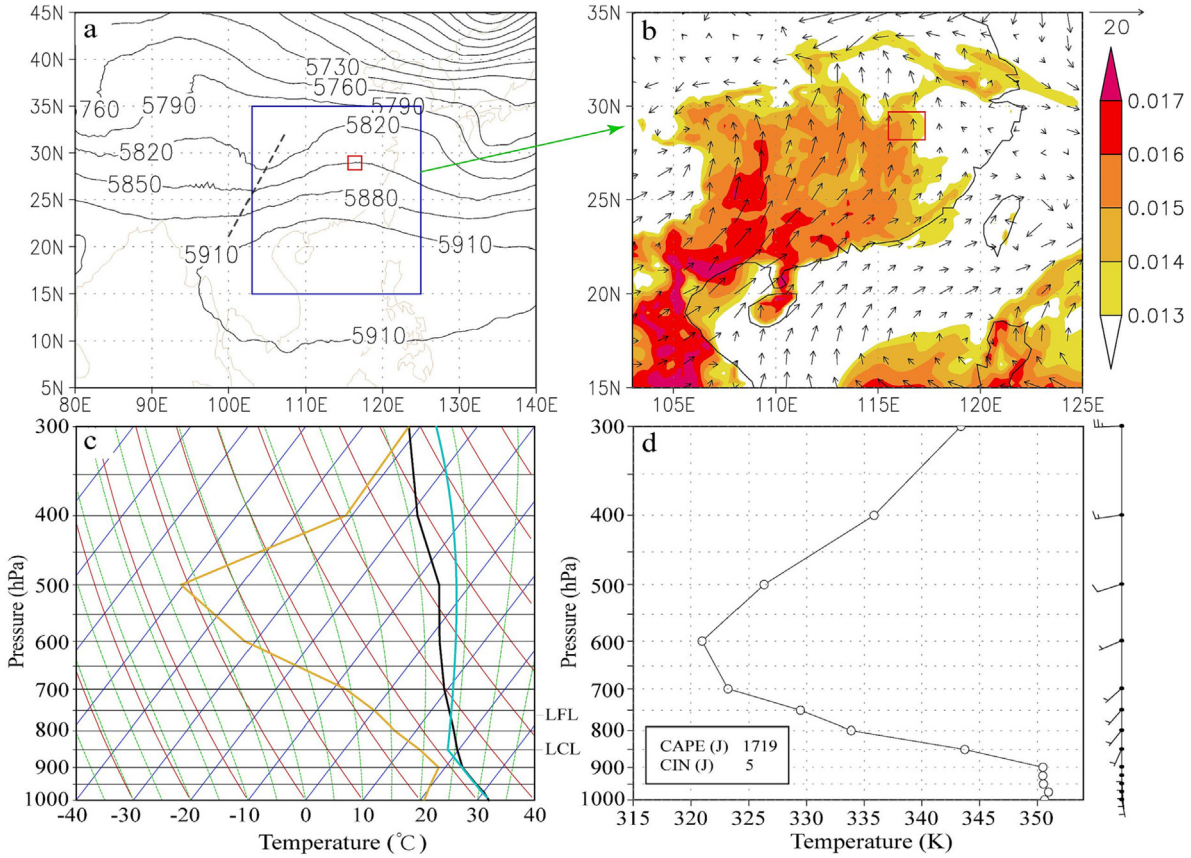

Fig. 4. (a) 500-hPa geopotential height (gpm), (b) 925-hPa wind (m s^{-1}) and specific humidity (kg kg^{-1}), and (c) *T*-log*P* diagram and (d) the profiles of pseudo-equivalent potential temperature (θ_{se}) and wind (the full and half wind barbs denote 4 and 2 m s − 1, respectively) over YX (29°N, 115.75°E) at 13:00 LST on 4 May 2020. The corresponding data are from ECMWF ERA5.

should be similar to that at 13:00 LST on 3 May 2020, as solar radiation, low-level temperature advection and evaporative cooling of precipitation were the important factors to determine lake surface temperature (Hostetler et al., 1993; Gu et al., 2015). It can be seen from Fig. 5a that PL is a cold source, and its surface temperature is about 4–12 °C lower than the surrounding land surface (Fig. 5a). Similar to the ECMWF ERA5 data, the airs around PL are dry with a temperature-dewpoint difference of >10 °C. Fig. 5a also shows that the 10-m winds in PL region are messy, and obviously different from the near-surface wind of ECMWF ERA5 (Fig. 4d), embodying the effect of the underlying surface on the near-surface ambient wind.

It can also be seen from Fig. 5a that the dominant winds over PL are southeasterly winds, and the wind speeds in the downstream region (i.e., the northwest of PL) are apparent larger than those in upstream, reflecting the small friction of the water surface. In the downstream region, the dewpoints are >23 °C and evidently larger than those in upstream region or other region (Fig. 5a), which is induced by the moistening of PL. Moreover, the 2-m air temperature near the shores of PL is lower than those of the areas far away from PL (Fig. 5a), indicating the cooling effect of PL. Fig. 5b depicted the evolution of 10-m wind and its zonal component at YX station from 00:00 LST to 23:00 LST on 4 May 2020. Before sunrise (about 05:30 LST), there was southwesterly wind, and after sunrise, the wind gradually turned to northeasterly wind or easterly wind, implying the lake-land breeze circulation.

4.3. Impacts of PL on temperature and humidity stratifications

PL affects the near-surface temperature and humidity, and then regulates the air temperature and humidity stratification of the atmosphere. The impacts of a lake on the temperature and humidity are mainly achieved through the water vapor and heat exchanges between the lake and its overlying air. Assuming a linear vertical profile of the sensible heat flux, the mean amount of heating by a lake for its overlying air in the mixed layer (Z) can be expressed (Markowski and Richardson, 2010; Zou et al., 2020) as,

$$\Delta\theta \approx \frac{1.2c_h L\overline{(\theta_0-\theta_a)}}{Z}, \quad (1)$$

where $c_h = 0.002$ is a bulk transfer coefficient for heating, θ_0 (θ_a) is the lake surface (2-m air) temperature, and L (km) is the distance of air traveling over a lake. Since there is southeasterly wind over PL, L (about 90 km) can be considered as the length of PL in southeast-northwest direction. The lake surface temperature θ_0 is about 28 °C, and the 2-m air temperature is about 34 °C (Fig. 5a). Suppose that the mixed layer Z is about 500 m over PL, Eq. (1) yields the mean heating of about 2.5 °C.

Meanwhile, supposing that the vertical profile of the water vapor flux is also linear, the mean amount of moistening by a lake for its overlying air in the mixed layer Z can be expressed (Markowski and Richardson, 2010; Zou et al., 2018) as,

$$\Delta r \approx \frac{0.4c_e L\overline{(r_0-r_a)}}{Z}, \quad (2)$$

where $c_e = 0.002$ is a bulk transfer coefficient for moistening, and r_0 (r_a) is the saturation water vapor mixing ratio at lake surface (2-m height). When calculating r_0, the lake surface temperature (i.e., 28 °C) is taken as the dewpoint, and r_0 is about 24 g kg^{-1}. The 2-m dewpoint (about 22.5 °C) in the upstream region (i.e., southeast) of PL is used to retrieve r_a, and r_a is about 17 g kg^{-1}. Therefore, Eq. (2) yields the mean moistening of about 1.0 g kg^{-1}, which is equivalent to increasing the average dewpoint by 1 °C in the mixed layer.

Since the heating and moistening of a lake on overlying air are gradually decreased with height in the mixed layer, it is assumed that the heating and moistening are decreased with height linearly. As a result, PL decreases air temperature near the surface (top of the mixed layer) by about 5 °C (0 °C), and increases dewpoint near the surface (top of the mixed layer) by about

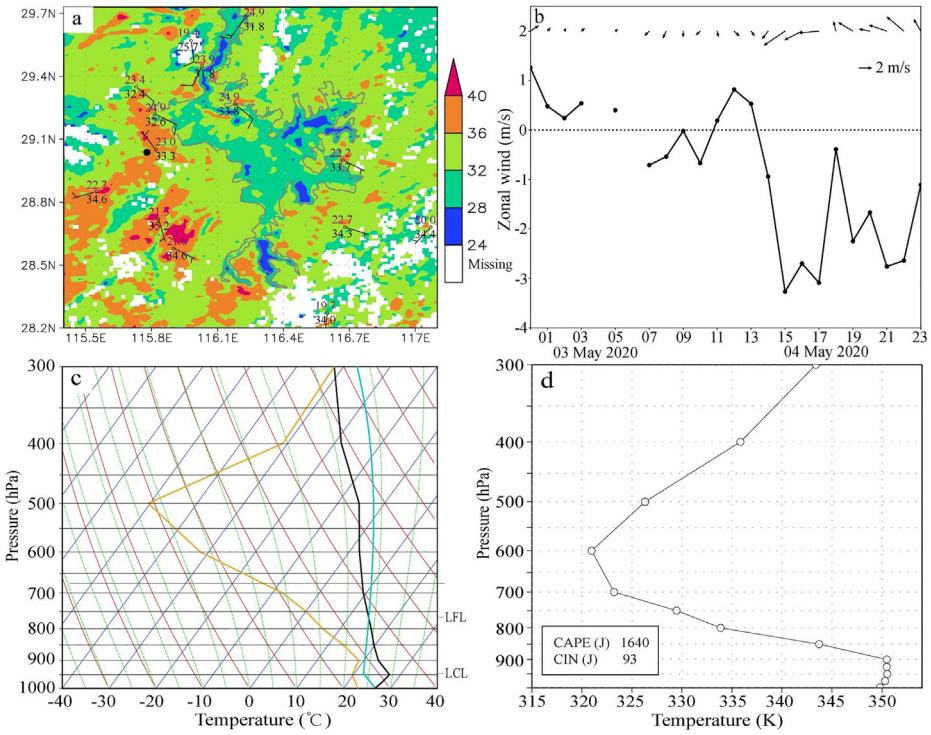

Fig. 5. (a) 2-m air temperature (black number; °C), 2-m dewpoint temperature (purple number; °C), 10-m wind (wind barb; the full and half wind barbs denote 4 and 2 m s^{-1}, respectively) at 13:00 LST on 4 May 2020 and MYD11A1 land surface temperature (shading; °C) at 13:30 LST on 3 May 2020. (b) the evolution of 10-m wind and its zonal component from 00:00 LST to 23:00 LST on 4 May 2020. (c) T-log$P$ diagram and (d) the profiles of pseudo-equivalent potential temperature (θ_{se}) over PL (i.e., the near-surface data in Fig. 4c are regulated by PL) at 13:00 LST on 4 May 2020. The black dot in (a) represents the location of convection initiation.

2 °C (0 °C). After amending the air temperature and humidity in the mixed layer over PL, the temperature and humidity stratifications also changes (Fig. 5c). The height of LCL is reduced remarkably, which is mainly caused by the increase of near-surface dewpoint. However, the cooling of PL increases the CIN by 93 J and slightly decreases the CAPE (Fig. 5d), which suggests that the development of convection over PL is more difficult than that over the surrounding land. Some studies have also pointed out that it is for this reason, a lake can weaken the crossing storm during daytime in the warm season owing to the reason (Metz, 2011; Workoff et al., 2012; Fu et al., 2013).

5. The WRF model simulation

The above observation analysis shows the impacts of PL on the near-surface air temperature, humidity and wind, as well as the vertical profiles of air temperature and humidity. However, since the observation data (especially for the west shore of PL) is sparse, the relation between the short-duration strong convection and PL is difficult to be revealed clearly. Therefore, numerical simulation is used to further explore and confirm the effect of PL on this strong short-duration convection.

5.1. Model configuration and numerical experimental design

The WRF model version 4.2 released in April 2021 is used in the current study. The model run with three one-way nested domains (D01, D02 and D03), and the largest domain (i.e., D01) is centered at (29.0°N, 116.3°E) with 181 × 161 grid points and the horizontal resolution of 15 km (Fig. 6a). The middle domain (D02) has 151 × 151 with the horizontal resolution of 5 km, while the innermost domain (D03) has 124 × 124 grid points with the horizontal resolution of 1.667 km.

In order to reveal the effect of PL on this convection, we set up 2 experiments: a control experiment with PL (CTL) and a sensitivity experiment without PL (SES-NOPL). In CTL experiment, the innermost domain (D03) includes the water body of PL (Fig. 6b), and the lake surface temperature has no change in space, but its time evolution is shown in Fig. 6c. Noted that introducing the time evolution of lake surface temperature can improve the simulation of convection over PL (Zou et al., 2023). In SES-NOPL experiment, the water body of PL in the innermost domain (D03) is replaced by arable land. The land surface types at each WRF model grids in other domains are the same between CTL and SES-NOPL experiments. CTL and SES-NOPL experiments share the same physical process (i.e., parameterization schemes). Grell–Freitas scheme is applied in D01, and no cumulus parameterization schemes are used in D02 and D03. Thompson microphysics scheme is used in all domains due to the advantage for simulating the precipitation in lake area (McMillen and Steenburgh, 2015), and the Unified Noah land-surface model is applied in the three domains owing to the better performance (Case, 2016; Gaur et al., 2021). The schemes of planetary boundary layer and long wave radiation are set to the Rapid Radiative Transfer Model and Yonsei University schemes, respectively. Moreover, CTL and SES-NOPL experiments are forced with the same initial and lateral boundary condition from the 6-hourly FNL data. Each experiment ran from 20:00 LST on 3 May to 20:00 LST on 4 May 2020, with the first 12 h for model spin-up. It is noted that the initial conditions of land surface and subsurface variables (e.g., land surface temperature, soil moisture, soil temperature, etc.) in CTL and SES-NOPL experiments are directly obtained through the interpolation from FNL data.

Both ECMWF ERA5 data and NCEP FNL data can effectively simulate the state of the atmosphere and changes in meteorological elements with space and time (Zhang et al., 2020; Wang et al., 2021). However, their horizontal resolutions have a large difference. The horizontal resolution of pressure-level data in ECMWF ERA5 is 0.25° × 0.25°, but that of land data (e.g., soil temperature, soil humidity, etc.) is 0.1° × 0.1°. By comparison, the horizontal resolution of NCEP FNL data (including pressure-level data and land data) is coarse, with 1° × 1°. Since the size of PL is about 0.6° × 0.6°, its signals have embedded into ECMWF ERA5 data, but not into NCEP FNL data (the area of PL is less than the corresponding area of one grid point). Although using ECMWF ERA5 data with high horizontal resolution to drive the CTL experiment may obtain more accurate results (Zhang et al., 2020), using it to drive the SES-NOPL experiment may result in abnormal results because the signals of PL in ECMWF ERA5 data are difficult to be removed. Despite there is no signal of PL in the initial condition of experiment driven by NCEP FNL data, the signal of PL will be transmitted to the overlying air through lake-air interaction. Therefore, the NCEP FNL data instead of ECMWF ERA5 data is selected as the initial and lateral boundary condition in this event.

5.2. Model validation

In order to indicate the performance of the WRF model in reproducing the strong short-duration convection near the west shore of PL on 4 May

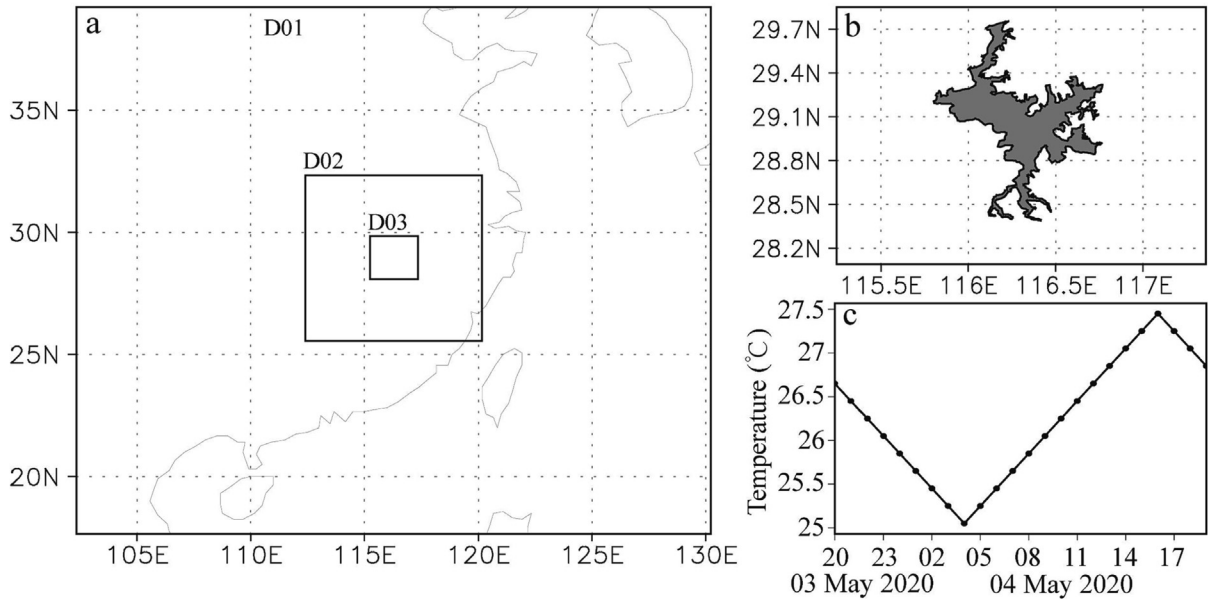

Fig. 6. (a) Locations of WRF model domains for all three-level nested domains, (b) the water body (shading) of PL in domain 3 (i.e., D03) and (d) the variation of lake surface temperature in domain 3.

2020, Fig. 7a–e shows the spatial distribution of the simulated maximum reflectivity over PL region in CTL experiment during this convection. At 13:00 LST on 4 May 2020, an isolated convection cell (i.e., cloud A) with the maximum reflectivity of about 30 dBZ occurred to the southwest side of PL (Fig. 7a), and its location was slightly south of the observation (Fig. 2a). Subsequently, the convection cell moved to toward northeast direction, and it gradually enhanced when closing to the west shore of PL. By 14:00 LST, the convection arrived at the west shore of PL with the maximum reflectivity >40 dBZ (Fig. 7b). At the same time, there were several isolated convection cells reoccurred at the raw location of convection initiation (i.e., the southwest side of PL). After that, the isolated convection cells to the southwest side of PL weakened and disappeared rapidly, while the convection cell near the west shore of PL rapidly enhanced and moved toward the northeast, and meanwhile, there were new convection cells initiated near the west shore of PL.

At 14:40 LST on 4 May 2020, the convection triggered near the west shore of PL (i.e., cloud B) developed to above 55 dBZ (Fig. 7c), which was equivalent to the observation (Fig. 2c). At this moment, the convection A moved into the main body of PL (Fig. 7c). The cross section of reflectivity along the black solid line in Fig. 7c showed that the echoes with reflectivity of >20 dBZ stretched up to 400 hPa, which was equivalent to a height of 7 km (Fig. 7f). Subsequently, the convections A and B continued to move toward northeast, and began to weaken quickly. By 15:00 LST on 4 May 2020, the intensity of convection A weakened to below 35 dBZ, and the intensity of convection B weakened to below 45 dBZ (Fig. 7d). At 15:40 LST on 4 May 2020, the convection A and B had disappeared, but there was also a new convection cell with reflectivity <35 dBZ near the west shore of PL (Fig. 7e). Soon after, no echoes with reflectivity >20 dBZ appeared over PL and its nearby areas (not shown), implying the end of the convection. Fig. 3b shows the averaged reflectivity in CTL experiment from 13:00 LST to 15:30 LST on 4 May 2020. The reflectivity of >5 dBZ was mainly located near west shore of PL, which was similar to the observation (Fig. 3a). Clearly, the CTL experiment has reasonably reproduced the strong short-duration convection near the west shore of PL, despite that there are some small differences in the location and intensity of the simulated and observed convection.

Fig. 8 gave the simulated temperature and humidity stratifications over YX and PL at 13:00 LST on 04 May 2020, as well as the profile of pseudo-equivalent potential temperature. Similar to the observation (Fig. 4c), the isotherm was approximately parallel to the low-level dry-adiabatic line over YX, and the relatively dry ambient appeared near 500 hPa, while the relatively moist ambient occurred between 900 hPa and 800 hPa. The values of CAPE (1639 J) and CIN (1 J) were also equivalent to those of the observation (Figs. 4d and 8d). Over PL, the near-surface air temperature decreased by about 5 °C, while the dewpoint increased by about 2 °C as compared with those over YX (Fig. 8c), which were consistent with the estimations of Eqs. (1) and (2). The changes of the near-surface air temperature and humidity over PL resulted in the decline of LCL, the decrease of CAPE, the increase of CIN and the enhancement of convective stability (Fig. 8c–d), which were also similar with the estimations of observation data (Fig. 5c–d). This further confirms the good performance of the WRF model. Therefore, it is reliable to explore the effects of PL on the strong short-duration convection with the output of the WRF model.

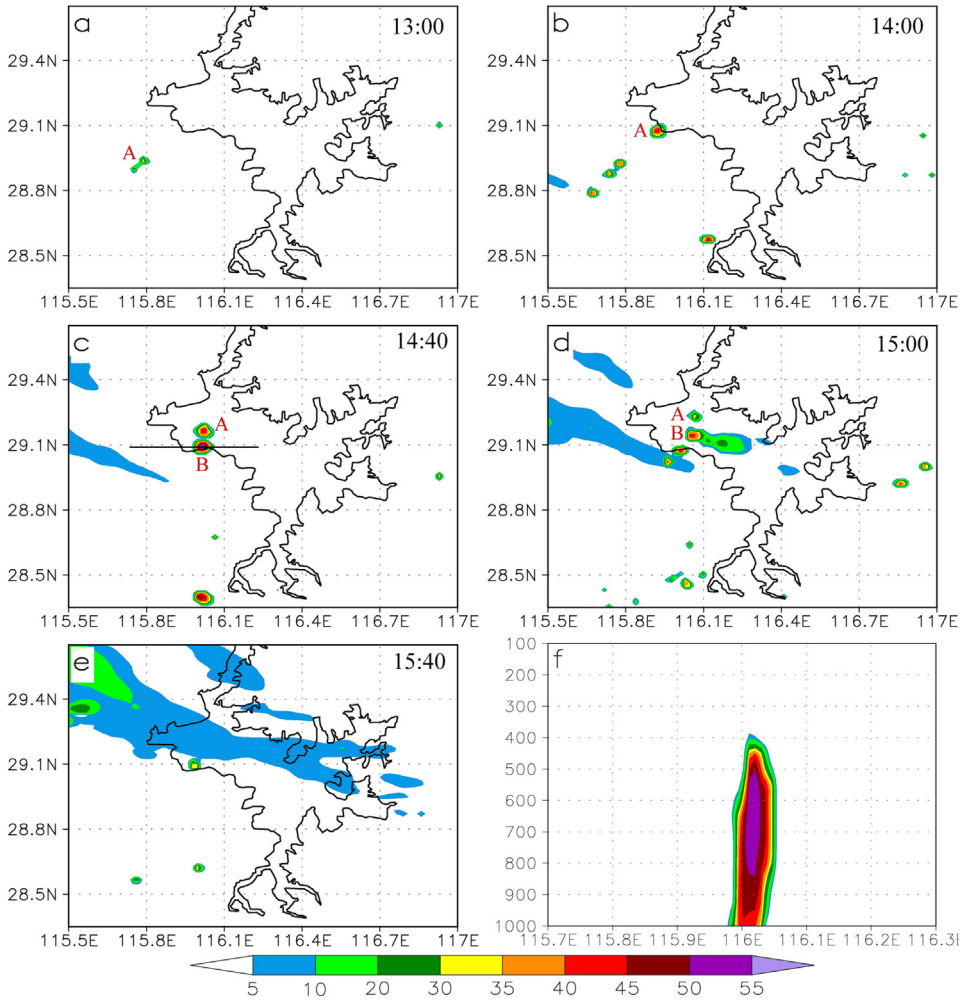

Fig. 7. The simulated maximum reflectivity (shading: dBZ) in domain D03 in CTL experiment at (a) 13:00 LST, (b) 14:40 LST, (c) 14:40 LST, (d) 15:00 LST and (e) 15:40 LST on 4 May 2020. (f) The cross section of reflectivity along the black solid line in (c).

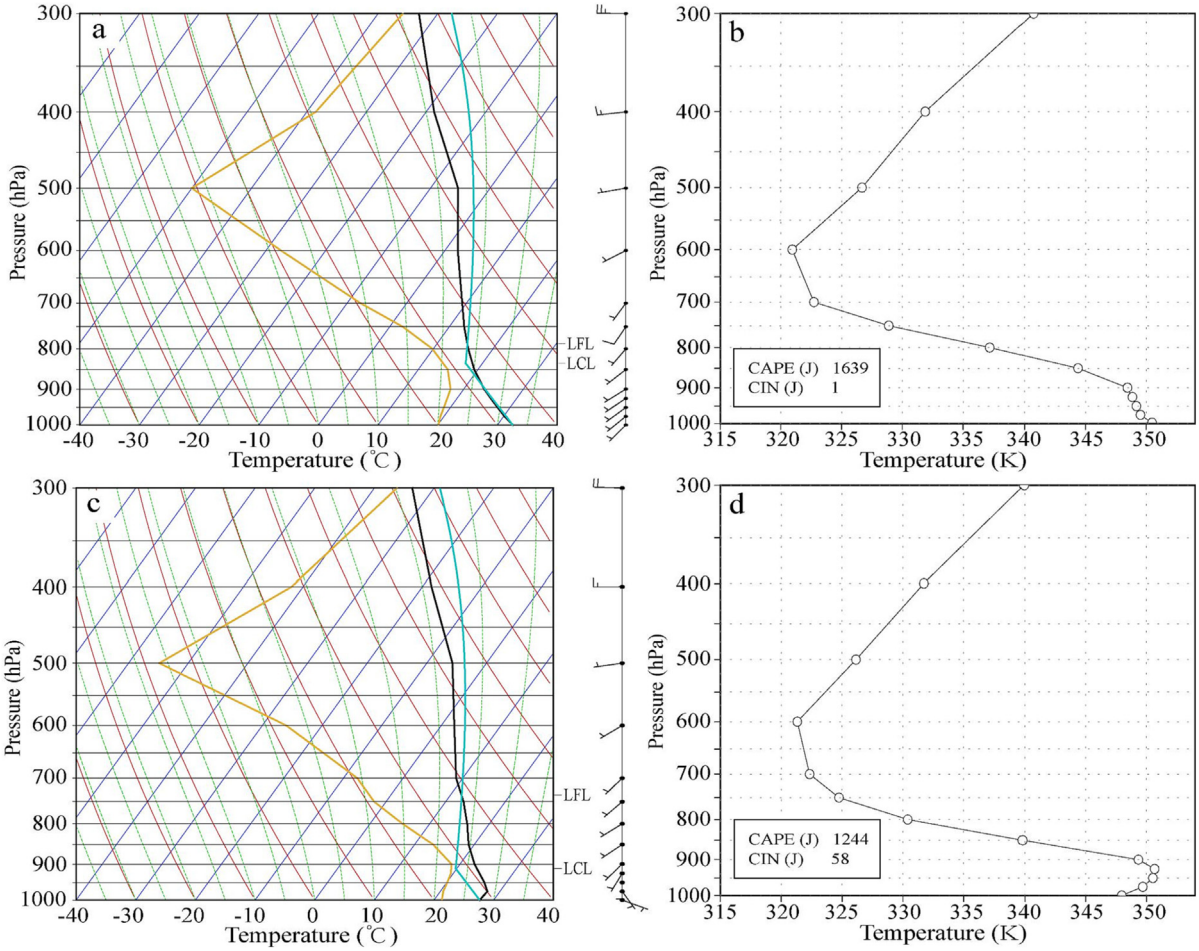

Fig. 8. (a, b) The *T*-log*P* diagram and the profiles of pseudo-equivalent potential temperature (θ_{se}) over YX (29°N, 115.75°E), and (c, d) over PL (29.15°N, 116.15°E) at 13:00 LST on 4 May 2020.

5.3. Impacts of PL on the strong short-duration convection

Fig. 7 showed the evolution of the simulated convection over PL and its nearby areas in CTL experiment. Similar to the observation, there was convection triggering over the southwest side of PL, and the convection rapidly enhanced when approaching the west shore of PL and quickly weakened and disappeared after entering the main body of PL. In SES-NOPL experiment, there were also isolated echoes initiating over the southwest side of PL (i.e., within black circle) at around noon on 4 May 2020 (Fig. 9a–b), but when moving toward northeast, they weakened and disappeared gradually (Fig. 9c). Thereafter, there were no obvious echoes developing on the west side of the main body of PL (Fig. 9d). The averaged reflectivity from 13:00 LST to 15:30 LST on 4 May 2020 also showed that there were isolated echoes to the southwest side of the PL's main body, but no obvious echoes appeared near the west shore of the PL's main body (Fig. 3c). This indicates that when the water body of PL is absent, there is still convection triggering over the southwest side of the PL's main body, but the convection weakened and disappeared gradually when moving toward the northeast. It is obvious that the initiation of the strong short-duration convection has not resulted from PL, but when it moves to the west shore of the PL's main body, its enhancement is induced by PL.

6. Possible mechanisms

When the convection approaches the west shore, how does PL strengthen it? Fig. 10a showed the distributions of 10-m wind and its divergence in CTL experiment at 13:00 LST on 4 May 2020. Obviously, southerly wind was the dominant wind outside PL, which was consistent with the ambient wind (Fig. 4d). However, the winds over PL and its shore were complex, and diverged from PL to the surrounding land, indicating the lake-land breeze circulation (Fig. 10a). The time-evolution difference in 10-m wind and its zonal component between YX (29°N, 115.75°E) and PL (29.15°N, 116.15°E) also reflected the lake-land breeze circulation (Fig. 10b). The lake-land breeze (easterly wind) in the west of PL and the ambient wind (southerly wind or southwesterly wind) to the southwest of PL converged in the vicinity of the west shore of PL, forming a strong convergence belt (Fig. 10a). When the convection moved over the convergence belt, it would be strengthened because of the strong uplifting movement in low level. Obviously, when the convection closed to the west shore of PL on 4 May 2020, its enhancement was mainly induced by the strong low-level convergence associated with lake-land breeze. This mechanism is similar to that of sea-land breeze inducing or enhancing convection/precipitation near the coastline around noon in warm season (Simpson et al., 2008; Shi et al., 2019; Hock et al., 2023).

In SES-NOPL experiment which the water body of PL was replaced by arable, the dominant winds over PL and its shore were southerly wind at 13:00 LST on 4 May 2020, and there was no obvious land-lake breeze circulation and convergence over PL and its nearby areas (Fig. 10c). The difference in 10-m wind between CTL and SES-NOPL experiments showed that there was an obvious divergence anomaly over PL (Fig. 10d). This evidence further confirms the presence of the lake-land breeze in CTL and the absence of that in SES-NOPL. This was the main reason why the convection in SES-NOPL experiment was not enhanced, when it closed to the west shore of PL (Fig. 9). Why does the lake-land breeze circulation occur in CTL instead of SES-NOPL? In fact, the low-level air tends to flow from a cool area to a warm area. Steenburgh et al. (2000) pointed out that a

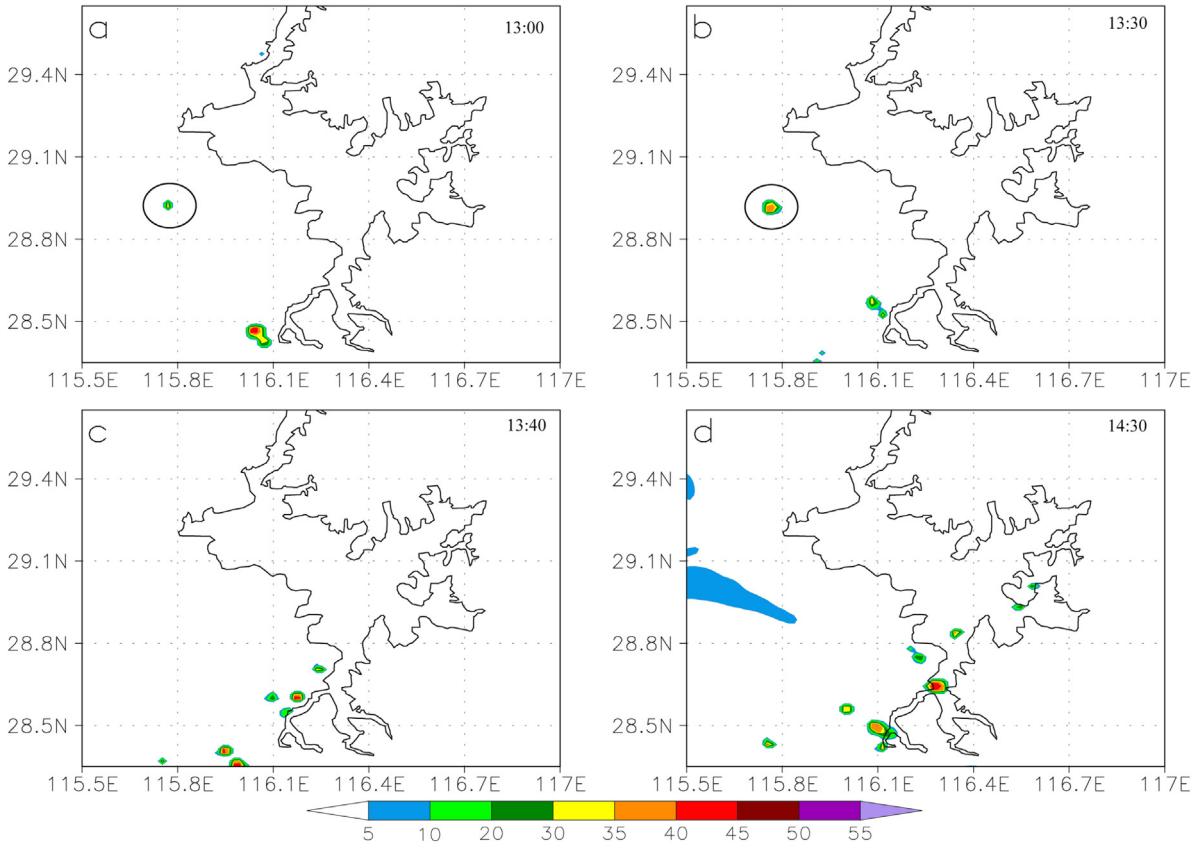

Fig. 9. The simulated maximum reflectivity (shading: dBZ) in domain D03 in SES-NOPL experiment at (a) 13:00 LST, (b) 13:30 LST, (c) 13:40 LST and (d) 14:30 LST on 4 May 2020.

temperature difference ≥ 4 °C between a lake and its nearby land was favorable for generating the lake-land breeze circulation. In CTL experiment, the land-lake temperature difference (land minus lake) was >8 °C at around 12:00 LST on 4 May 2020 (not shown), which was responsible for the generation of lake-land breeze circulation. However, in SES-NOPL experiment, the land-lake temperature difference was about 2 °C (not shown), which was not instrumental in the production of lake-lake breeze circulation.

Fig. 10a and c showed that whether the water body of PL was replaced by arable, there was always a strong low-level wind convergence belt with southwest-northeast direction in the southwest side of PL (i.e., within the red rectangle) at 13:00 LST on 4 May 2020, and this convergence belt was responsible for the initiation of convection in the southwest side of PL in CTL and SES-NOPL experiments (Figs. 7a and 9a). Fig. 10d also showed that the 10-m wind and its divergence have no obvious difference between CTL and SES-NOPL experiments in this region, which implied that the occurrence of the convergence belt in the southwest side of PL was not markedly related to PL.

How does this convergence belt form? In order to reveal it, the 10-m wind in the red rectangles in Fig. 10a–b is enlarged into Fig. 11a–b, and the corresponding topography is also embedded. Similar to Fig. 10d, there was no obvious difference in 10-m wind between CTL and SES-NOPL experiments. The area south of Meiling Mountain was mainly controlled by southerly wind (Fig. 11a–b). When the air passed through Meiling, it was divided into two parts. One part climbed over Meiling and maintained southerly wind, and the other part flowed along the north boundary of Meiling and formed southwesterly wind in the north of Meiling (Fig. 11a–b). The southerly wind (over Meiling) and the southwesterly wind (north of Meiling) converged in the north of Meiling (Fig. 11a–b), forming the strong low-level wind convergence with the southwest-northeast direction (Fig. 10a–b). Along this convergence, a strong upward motion zone with a maximal velocity >0.6 m s^{-1} occurred at 975 hPa, and the strong short-duration convection was triggered in the strong upward motion zone (Fig. 11a–b).

The above analysis indicates that the southwesterly wind near the north boundary of Meiling plays an important role to produce the strong low-level wind convergence, the strong upward motion zone, and even the convection initiation. How does it form? In fact, mountains can not only strengthen precipitation in windward slope (Zhao et al., 2022; Chutiman et al., 2022), but also generate flow around them (Bauer et al., 2000; Wang and Tan, 2006; Jagannathan et al., 2019). Is this southwesterly wind parallel to the north boundary of Meiling induced by Meiling itself? In order to confirm this problem, we also conduct a new sensitivity experiment removing Meiling based on SES-NOPL experiment (SES-NOPLML), in which the terrain height of Meiling is uniformly reduced to below 30 m, and the revised topography is shown in Fig. 10c. This design of SES-NOPLML is similar to that of Lin and Sheng (2019) to reveal the influence of topography on extreme rainfall. Fig. 11c showed the 10-m wind and 975-hPa upward velocity near Meiling in SES-NOPLML at 13:00 LST on 4 May 2020, and there was no obvious southwesterly wind and convergence, as well as low-level upward motion. As a result, SES-NOPLML did not trigger any convection near Meiling from 13:00 LST to 15:30 LST on 4 May 2020 (Fig. 3d). The differences of 10-m wind and 975-hPa vertical velocity between SES-NOPL and SES-NOPLML (SES-NOPL minus SES-NOPLML) also showed that there were strong 10-m wind convergence and strong upward motion near north of Meiling (Fig. 11d), which were quite similar with those in SES-NOPL and CTL (Fig. 11a–b). These evidences clearly indicate that the southwesterly wind, low-level convergence belt, low-level upward motion zone and convection initiation near north boundary of Meiling on 4 May 2020 were mainly induced by the Meiling, and the main role of Meiling was to make the air near the northern boundary flow around it (Fig. 11d). In fact, Bauer et al. (2000), Wang and Tan (2006) and Jagannathan et al. (2019) indicated that mountain can often induce such airflow around it.

Since the presence of the lake-land breeze, the 10-m wind over the main body of PL does not converge, but rather than diverges evidently (Fig. 10a and d), which is beneficial for weakening convection over the main body of

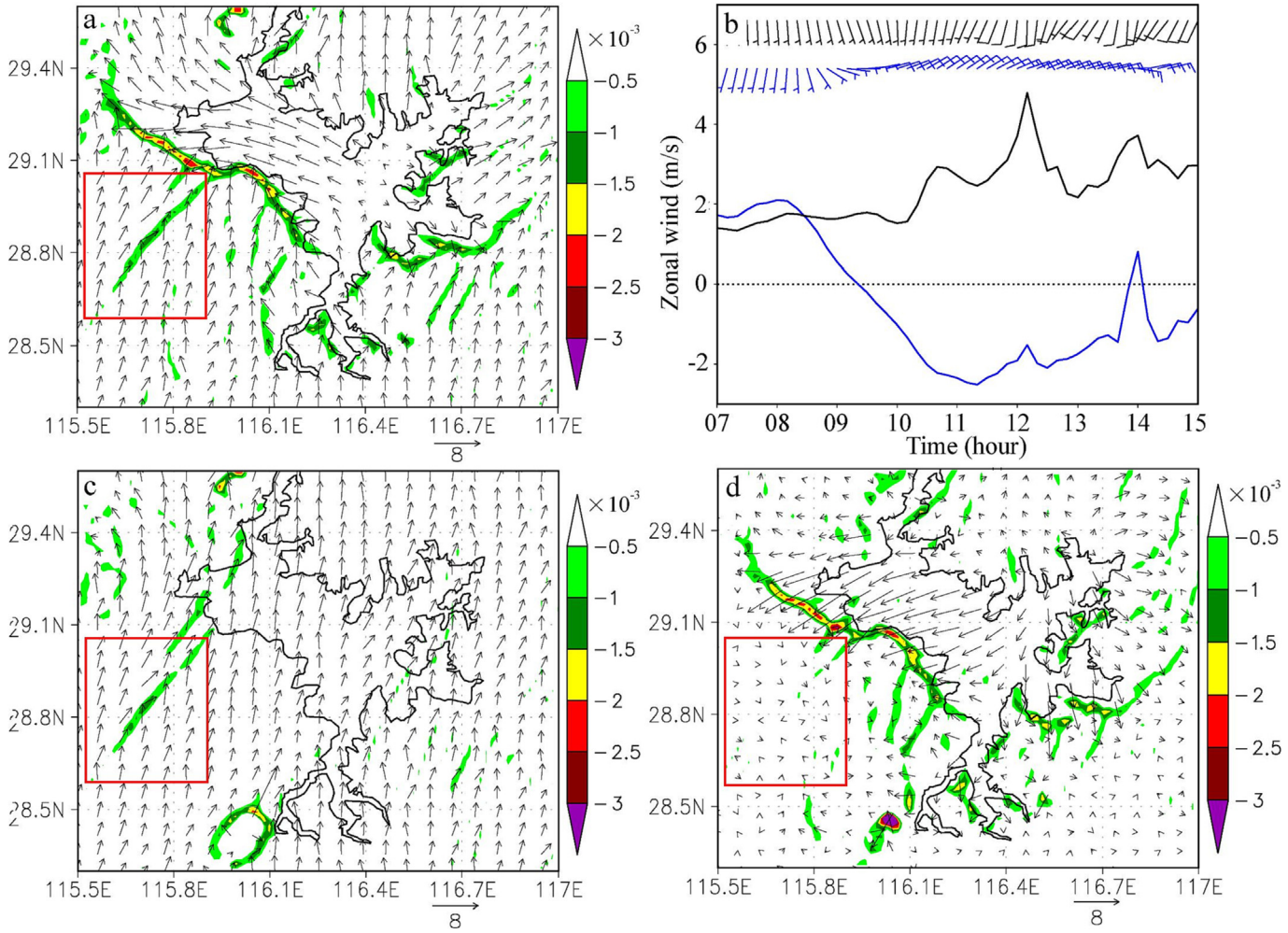

Fig. 10. The 10-m wind (arrows, m s^{-1}) and its divergence (shadowing, s^{-1}) in (a) CTL experiment and (c) SES-NOPL experiment, and (d) the differences in 10-m wind and its divergence between CTL and SES-NOPL experiments at 13:00 LST on 4 May 2020. (b) the evolutions of 10-m wind and its zonal component over YX (29°N, 115.75°E; the black arrows and line) and PL (29.15°N, 116.15°E; the blue arrows and line) in CTL.

PL. Moreover, owing to the cooling of PL, the CIN and convective stability over the main body of PL are increased obviously compared with those over the land in the southwest of PL (Fig. 8), which indicates that the development and maintenance of convection over PL is more difficult than that over nearby land because of the increase of energy required for near-surface air to lift to above LFC. Therefore, when the convection enters the main body of PL from the vicinity of the southwest shore of PL, it would weaken and disappear gradually due to the decrease of low-level uplifting and the increases of CIN and convective stability. This was the main reason why the convection on 4 May 2020 weakened and disappeared rapidly after entering the main of PL (Figs. 2 and 7). The mechanism of the convection weakening is analogous to the studies of Metz (2011) and Fu et al. (2013).

7. Summary and discussion

Lake usually suppresses the development of convection in the lake region during the daytime of warm season and weakens the storm crossing it (Metz, 2011; Fu et al., 2013; Gu et al., 2016; Wu et al., 2019; Zou, 2020). However, at around 13:30 LST on 4 May 2020, a convection was triggered at about 20 km west from the west shore of PL under the favorable large-scale environmental conditions, and strengthened rapidly when approaching the west shore of PL, and then weakened and disappeared quickly after entering the main body of PL. Although the convection only lasted about 2 h, its maximal reflectivity exceeded 55 dBZ and echo-top height was up to about 12 km, and resulted in lightning, threatening the safety of people's lives and property in PL region and the operation of transportation on PL. In this paper, the formation mechanism of the strong short-duration convection is examined based on the observational data and the numerical simulation based on the WRF model.

By diagnosing the impacts of PL on the air temperature and humidity, and comparing the result from the SES-NOPL experiment without PL (PL is replaced by arable) with the result from CTL experiment with PL, we revealed the contribution of PL to the strong short-duration convection. Specifically, the enhancement of the convection is mainly induced by PL when it approaches the west shore of PL, and the weakening and disappearing of the convection is also resulted from PL when it enters the main body of PL. However, the initiation of the convection is not closely related to PL, and it is mainly induced by the local topography (i.e., Meiling).

The main physical mechanism of the local topography affecting the initiation of the convection is that when the prevailing southerly wind south of the Meiling passes through it, the wind was separated into two parts by the role of topography. One part climbs over topography and continues to maintain southerly wind, while the other part flows along the north boundary of Meiling, forming southwesterly wind. The southerly wind passing over Meiling and the southwesterly wind along the north boundary of Meiling converge in the north of Meiling, and produce strong convergence of low-level wind, finally triggering the convection under the favorable large-scale environmental conditions (Fig. 12a).

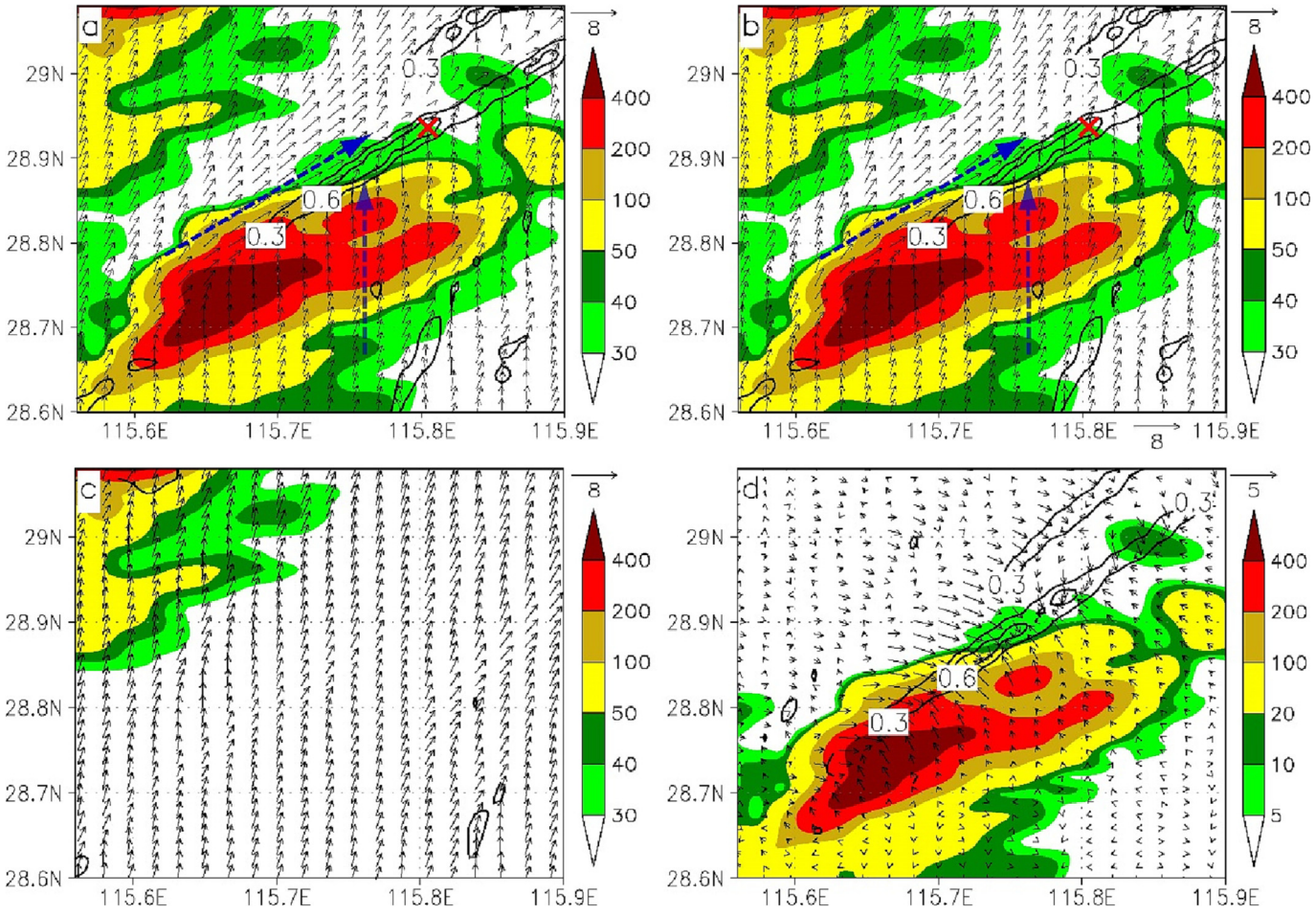

Fig. 11. The altitude (shadowing, m), 10-m wind (arrows, m s^{-1}) and 975-hPa vertical velocity (black solid line, m s^{-1}) within the red rectangle region in Fig. 9a in (a) CTL, (b) SES-NOPL, (c) SES-NOPLML and (d) their differences between SES-NOPL and SES-NOPLML (SES-NOPL minus SES-NOPLML) at 13:00 LST on 4 May 2020. The red crosses in (a) and (b) denote the initiation location of the simulated convection.

At around noon (i.e., the convection is triggered in this period), PL is obviously cooler than the surrounding land, and the large surface temperature difference between lake and the surrounding land results in lake-land breeze, which makes the near-surface air over PL flow to the surrounding land. In the west of PL, the lake-land breeze is presented as northeasterly wind. As a result, the southwesterly wind from the north of the Meiling and the northeasterly wind from the west of PL met in the vicinity of the west shore of PL, forming a strong convergence belt. Under the steering of southwesterly wind in high level, the convection triggered at the north of the Meiling moves to northwest. When the convection approaches the west shore of PL, the strong uplifting associated with the convergence belt induces to the rapidly enhancement of the convection (Fig. 12b).

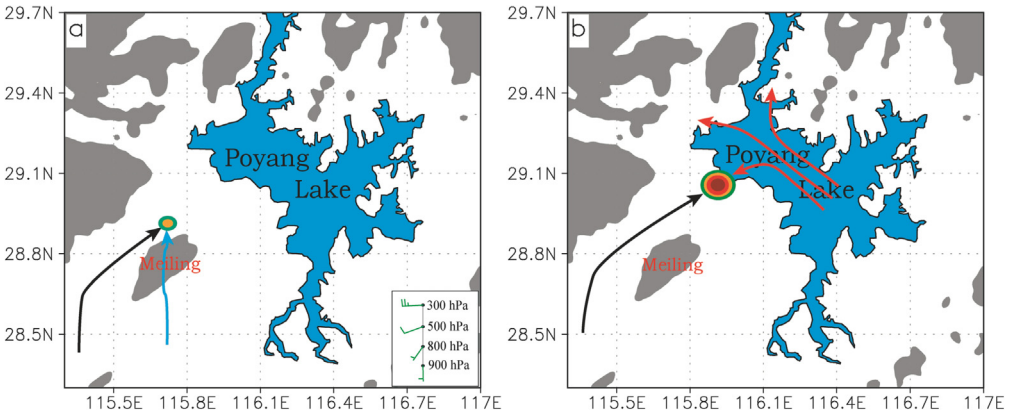

Fig. 12. Schematic diagram of the influence mechanisms of the strong short-duration convection on 4 May 2020, and (a) for the convection initiation and (b) for the convection enhancement. Gray shadowing represents the topography with an altitude of >100 m. The black arrow denotes the low-level wind flowing around Meiling, and blue arrow indicates the low-level wind flowing over the Meiling. Red arrows denote the low-level wind affected by PL, and colored circle indicates the location and intensity of convection.

Over the main body of PL, the lake-land breeze is dominant wind, and the near-surface wind emerges divergence instead of convergence, favoring for the subsidence in low level. In addition, since the cooling of PL, the temperature of overlying air is decreases, resulting to the decrease of CAPE and the increases of CIN and convective stability, which increases the difficult to maintain and develop the convection. Therefore, when the convection moves from the west shore of PL to the main body of PL, the divergence of near-surface wind associated with the lake-land breeze and the enhanced atmospheric stability jointly induce the rapid weakening and disappearing of the convection.

This study has revealed the formation mechanism of the strong short-duration convection occurred near the west shore of PL at around noon on 4 May 2020. The lake-land breeze over PL was responsibility for the rapid enhancement of the convection when approaching the vicinity of west shore of PL, and the Meiling Mountain in southwest of PL played an important role in the initiation of the convection. However, the conclusions are originated from one case, and more case studies are necessary for the generalizability of the conclusions. Moreover, in order to improve the forecast skill of such convection near PL, the favorable large-scale conditions (weather patterns, lapse rate, CAPE, etc.) for such convection (including convection triggered by Meiling Mountain) also should be revealed in the future work.

CRediT authorship contribution statement

Haibo Zou and Anning Huang conceived and designed the study. Landi Zhong and Shanshan WU were involved in data collection. Haibo Zou and Miaoxia Tian analyzed the data and prepared the figures and tables. Haibo Zou and Miaoxia Tian wrote the manuscript, and all coauthors approved it.

Data availability statement

The authors are grateful to Nanchang Meteorological Bureau in China for providing the radar data, conventional meteorological observation data and lighting data, and NASA for providing the MODIS land surface temperature product (MYD11A1; available at https://modis.gsfc.nasa.gov/data/dataprod/mod11.php). Due to confidentiality agreements, the radar data, conventional meteorological observation data and lighting data can only be made available to bona fide researcher subject to a non-disclosure agreement. Details of these data and how to request access are available from the Meteorological Information Center of Jiangxi Province in China, or the National Meteorological Information Center in China (http://data.cma.cn). The fifth-generation ECMWF atmospheric reanalysis (ERA5) are available online (https://climate.copernicus.eu/climate-reanalysis). The NCEP FNL data are obtained from https://rda.ucar.edu/datasets/ds083.2/index.html.

Declaration of competing interest

The authors declare that they have no known competing financial interests or personal relationships that could have appeared to influence the work reported in this paper.

Acknowledgments

This material is jointly supported by the National Science Foundation of China (42275007 and 41865003), the Natural Science Foundation Project of Jiangxi Province in China (20224BAB203045) and Key Lab of Poyang Lake Wetland and Watershed Research of Ministry of Education (Jiangxi Normal University) (PK2022005).

References

Alcott, T., Steenburgh, W., Laird, N., 2012. Great salt lake-effect precipitation: observed frequency, characteristics, and associated environmental factors. Weather Forecast. 27, 954–971.
Angel, J.R., Isard, S.A., 1998. The frequency and intensity of Great Lake cyclones. J. Clim. 11, 61–71.
Bauer, M.H., Mayr, G.J., Vergeiner, I., Pichler, H., 2000. Strongly nonlinear flow over and around a three-dimensional mountain as a function of the horizontal aspect ratio. J. Atmos. Sci. 57, 3971–3991.
Carpenter, D., 1993. The Lake effect of the great salt lake: overview and forecast problems. Weather Forecast. 8, 181–193.
Case, J., 2016. From drought to fooding in less than a week over South Carolina. Results Phys. 1183–1184.
Chutiman, N., Chiangpradit, M., Kong-ied, B. Daily Maximum, et al., 2022. Rainfall forecast affected by tropical cyclones using Grey theory. Civ. Eng. J. 1565–1573.
Dai, Y., Chen, D., Yao, T., Wang, L., 2020. Large lakes over the Tibetan Plateau may boost snow downwind: implications for snow disaster. Sci. Bull. 65, 1713–1717.
Dibs, H., Ali, A.H., Al-Ansari, N., et al., 2023. Fusion Landsat-8 thermal TIRS and OLI datasets for superior monitoring and change detection using remote sensing. Emerg. Sci. J. 7, 428–444.
Dockus, D., 1985. Lake effect snow forecasting in the computer age. Natl. Weather Dig. 10, 5–19.
Du, Y., Chen, G., 2019. Heavy rainfall associated with double low-level jets over southern China. Part II: convection initiation. Mon. Weather Rev. 147, 543–565.
Duan, H., Zhou, H., Xia, X., et al., 2020. Analysis of lightning activity law in Jiangxi Province in the last 15 years using ADTD data. Meteorol. Disaster Reduction Res. 39, 133–135 (in Chinese).
Fu, M.N., Zheng, Y.F., Zou, H.B., et al., 2013. Analysis on weakening process of convective system passing over Poyang Lake in summer. Plateau Meteorol. 32, 865–873 (in Chinese).
Gaur, A., Lacasse, M., Armstrong, M., et al., 2021. Effects of using different urban parametrization schemes and land-cover datasets on the accuracy of WRF model over the City of Ottawa. Urban Clim. 35, 100737.
Gu, H., Jin, J., Wu, Y., et al., 2015. Calibration and validation of lake surface temperature simulations with the coupled WRF-lake model. Clim. Chang. 129, 71–483.
Gu, H.P., Ma, Z.G., Li, M.X., 2016. Effect of a large and very shallow lake on local summer precipitation over the Lake Taihu basin in China. J. Geophys. Res. Atmos. 121, 8832–8848.
Hjelmfelt, M., 1990. Numerical study of the influence of environmental conditions on lake-effect snowstorms over Lake Michigan. Mon. Weather Rev. 118, 138–150.
Hock, N., Zhang, F., Pu, Z., 2023. Numerical simulations of a Florida sea breeze and its interactions with associated convection: effects of geophysical representations and model resolution. Adv. Atmos. Sci. 39, 697–713.
Hostetler, S., Bates, G., Giorgi, F., 1993. Interactive coupling of a lake thermal model with a regional climate model. J. Geophys. Res. 98, 5045–5057.
Huziy, O., Teufel, B., Sushanma, L., et al., 2021. Heavy lake-effect snowfall changes and mechanism for the laurentian Great Lakes Region. Atmosphere 12, 1577.
Jagannathan, A., Winters, K., Armi, L., 2019. Stratified flows over and around long dynamically tall mountain ridges. J. Atmos. Sci. 76 (5), 1265–1287.
Javadinejad, S., Dara, R., Jafary, F., 2020. Climate change scenarios and effects on snow-melt runoff. Civ. Eng. J. 6, 1715–1725.
Kristovich, D., Spinar, M., 2005. Diurnal variations in lake-effect precipitation near the western Great Lakes. J. Hydrometeorol. 6, 210–218.
Kristovich, D.A.R., Bard, L., Stoecker, L., 2018. Influence of Lake Erie on a Lake Ontario lake-effect snowstorm. J. Appl. Meteorol. Climatol. 57, 2019–2033.
Laird, N., Bentley, A., Ganetis, S., Stieneke, A., Tushaus, S., 2016. Climatology of lake-effect precipitation events over Lake Tahoe and Pyramid Lake. J. Appl. Meteorol. Climatol. 55, 297–312.
Lang, C.E., McDonald, J.M., Gaudet, L., et al., 2018. The Influence of a lake-to-lake connection from Lake Huron on the lake-effect snowfall in the vicinity of Lake Ontario. J. Appl. Meteorol. Climatol. 57, 1423–1439.
Li, Y.L., Yao, J., Zhang, X.L., et al., 2017. Study on the vertical stratification in Poyang Lake. Resour. Environ. Yangtze Basin 26, 915–924 (in Chinese).
Li, K., Guan, K., Jiang, C., et al., 2021. Evaluation of four new land surface temperature (LST) products in the US Corn Belt: ECOSTRESS, GOES-R, Landsat, and Sentinel-3. IEEE J. Sel. Top. Appl. Earth Obs. Remote Sens. 14, 9931–9945.
Lin, C., Sheng, L., 2019. Numerical analysis of the mesoscale dynamics of an extreme rainfall and flood event in Sri Lanka in May 2016. J. Meteorol. Soc. Jpn. 97, 821–839.
Ma, Y., Han, C., Zhong, L., et al., 2014. Using MODIS and AVHRR data to determine regional surface heating field and heat flux distributions over the heterogeneous landscape of the Tibetan Plateau. Theor. Appl. Climatol. 117, 643–652.
Markowski, P., Richardson, Y., 2010. Mesoscale instabilities. In: Markowski, P., Richardson, Y. (Eds.), Mesoscale Meteorology in Midlatitudes. John Wiley & Sons, Ltd, Chichester, West Sussex, UK 97 pp.
McMillen, J.D., Steenburgh, W.J., 2015. Impact of microphysics parameterizations on simulations of the 27 October 2010 Great Salt Lake-effect snowstorm. Weather Forecast. 30, 136–152.
Metz, N.D., 2011. Persistence and Dissipation of Lake Michigan Crossing Mesoscale Convective Systems. Ph.D. dissertation,University at Albany, State University of New York, Albany, NY 237 pp.
Miner, T., Fritsch, J., 1997. Lake-effect rain events. Mon. Weather Rev. 125, 3231–3248.
Nicosia, D., Ostuno, E., 1999. A flash flood from a lake-enhanced rainband. Weather Forecast. 14, 271–288.
Nordbo, A., Launiainen, S., Mammarella, I., et al., 2011. Long-term energy flux measurements and energy balance over a small boreal lake using eddy covariance technique. J. Geophys. Res. Atmos. 116, D02119.
Owens, N.D., Rauber, R.M., Jewett, B.F., et al., 2017. The contribution of lake enhancement to extreme snowfall within the Chicago–Milwaukee urban corridor during the 2011 Groundhog Day blizzard. Mon. Weather Rev. 145, 2405–2420.
Rodriguez, Y., Kristovich, D.A.R., Hjelmfelt, M.R., 2007. Lake-to-lake cloud bands: frequencies and locations. Mon. Weather Rev. 135, 4202–4213.
Rose Jr., B.L., 2001. The Role of Upstream Lakes in Determining Downstream Severe Lake-Effect Snowstorms. Ph.D. dissertationUniversity of Illinois at Urbana–Champaign, Champaign 182 pp.

Ruhf, R.J., Cutrim, E.M.C., 2003. Time series analysis of 20 years of hourly precipitation in southwest Michigan. J. Great Lakes Res. 29 (2), 256–267.
Schroeder, J.J., Kristovich, D.A.R., Hjelmfelt, M.R., 2006. Boundary layer and microphysical influences of natural cloud seeding on a lake-effect snowstorm. Mon. Weather Rev. 134, 1842–1858.
Shankman, D., Keim, B.D., Nakayama, T., et al., 2012. Hydroclimate analysis of severe floods in China's Poyang Lake region. Earth Interact. 16, 1–16.
Shi, R., Cai, Q., Dong, L., et al., 2019. Response of the diurnal cycle of summer rainfall to large-scale circulation and coastal upwelling at Hainan, South China. J. Geophys. Res. Atmos. 124, 3702–3725.
Simpson, M., Raman, S., Suresh, R., et al., 2008. Urban effects of Chennai on sea breeze induced convection and precipitation. J. Earth Syst. Sci. 117, 897–909.
Steenburgh, W.J., Halvorson, S.F., Onton, D.J., 2000. Climatology of lake-effect snowstorms of the Great Salt Lake. Mon. Weather Rev. 128, 709–727.
Steiger, S., Hamilton, R., Keeler, J., Orville, R., 2009. Lake-effect thunderstorms in the lower Great Lakes. J. Appl. Meteorol. Climatol. 48, 889–902.
Stepanenko, V.M., Joehnk, K.D., Maxhulskaya, E., et al., 2014. Simulation of surface energy fluxes and stratification of a small boreal lake by a set of one-dimensional models. Tellus A: Dyn. Meteorol. Oceanogr. 66, 21389.
Su, D.S., Wen, L.J., Zhao, L., et al., 2019. Numerical simulation of seasonal local climate effect in Qinghai Lake. Plateau Meteor. 38, 944–958 (in Chinese).
Wang, Q., Tan, Z., 2006. Flow regimes for major topographic obstacles of China. Chin. J. Geophys. 49, 971–982 (in Chinese).
Wang, W., Xiao, W., Cao, C., et al., 2014. Temporal and spatial variations in radiation and energy balance across a large freshwater lake in China. J. Hydrol. 511, 811–824.
Wang, X., Li, L., Gong, K., et al., 2021. Modelling air quality during the EXPLORE-YRD campaign – part I. Model performance evaluation and impacts of meteorological inputs and grid resolutions. Atmos. Environ. 246, 118131.
Workoff, T., Kristovich, D., Laird, N., et al., 2012. Influence of the Lake Erie over lake boundary layer on deep convective storm evolution. Weather Forecast. 27, 1279–1289.
Wright, D., Posselt, D., Steiner, A., 2013. Sensitivity of lake-effect snowfall to lake ice cover and temperature in the Great Lakes Region. Mon. Weather Rev. 141, 670–689.
Wu, Y., Huang, A., Yang, B., et al., 2019. Numerical study on the climatic effect of the lake clusters over Tibetan Plateau in summer. Clim. Dyn. 53, 5215–5236.
Wu, Y., Huang, A., Lazhu, et al., 2020. Improvements of the coupled WRF-Lake model over Lake Nam Co, Central Tibetan Plateau. Clim. Dyn. 55, 2703–2724.
Xiao, C., Lofgren, B., Wang, J., et al., 2018. A dynmical downscaling progection of future climate change in the laurentian Great Lakes region using a coupled air-lake model. Preprints 2018070468.
Xu, J., Ma, Y.M., Sun, F.L., et al., 2018. Analysis of effects of lake and upstream orography on the precipitation in fall over Nam Co Area. Plateau Meteor. 37, 1535–1543 (In Chinese).
Zhang, B., Wu, Y., Zhao, B., et al., 2022. Progress and challenges in intelligent remote sensing satellite systems. IEEE J. Sel. Top. Appl. Earth Obs. Remote Sens. 15, 1814–1822.
Zhang, Y., Chen, J., Tang, B., et al., 2020. Numerical simulation of meteorological elements of a pollution episode in Sichuan Basin based on two reanalysis datasets. Acta Sci. Circumst. 40, 3093–3102 (in Chinese).
Zhao, Z., Huang, A., Ma, W., et al., 2022. Effects of Lake Nam Co and surrounding terrain on extreme precipitation over Nam Co basin, Tibetan Plateau: a case study. J. Geophys. Res. Atmos. 127 e2021JD036190.
Zou, H., 2020. Statistical Analysis and Case Study of Lake-Effect Precipitation Over Poyang Lake. Ph.D. dissertation,Lanzhou University, Lanzhou, China, p. 237.
Zou, H.B., Zhang, S.W., Liang, X.D., et al., 2018. Improved algorithms for removing isolated non-meteorological echoes and ground clutters in CINRAD. J. Meteorol. Res. 32, 584–597.
Zou, H.B., Zhang, S.W., Liu, Y.N., et al., 2020. Analysis of a convective storm crossing Poyang Lake in China. J. Meteorol. Res. 34, 529–545.
Zou, H.B., Wu, S.S., Shan, J.S., 2022. Sensitivity of lake-effect convection to the lake surface temperature over Poyang Lake in China. J. Meteorol. Res. 36, 342–359.
Zou, H.B., Tian, M.X., Bin, Z., Wu, S.S., 2023. Impacts of spatiotemporal variation in lake surface temperature on a convection over Poyang Lake. J. Atmos. Sol. Terr. Phys. 245, 106048.